Opto-Electronic Advances

Supplementary information

2022, Vol. 5, No. 7

DOI: 10.29026/oea.2022.200097

Dual bound states in the continuum enhanced second harmonic generation with Transition Metal Dichalcogenides monolayer

Peilong Hong[1]*, Lei Xu[2]* and Mohsen Rahmani[2]

[1]School of Optoelectronic Science and Engineering, University of Electronic Science and Technology of China (UESTC), Chengdu 611731, China; [2]Advanced Optics & Photonics Laboratory, Department of Engineering, School of Science & Technology, Nottingham Trent University, Nottingham NG11 8NS, UK.

*Correspondence: PL Hong,E-mail: plhong@uestc.edu.cn; L Xu, E-mail: lei.xu@ntu.ac.uk

This file includes:

Supplementary information for this paper is available at https://doi.org/10.29026/oea.2022.200097

Section 1: Simulation methods

The full wave simulations were done with the frequency domain in COMSOL Multiphysics. For the modeled grating slab, the size of the grating strip along the y axis is assumed infinite. Periodic boundary conditions were implemented at the boundary of the unit cell of the grating along the x direction. Along the z direction, perfectly matching layers were implemented at the boundary of free space. The band structures and quality factors were calculated by using the eigenvalue solver. To calculate the SHG signals, we first did full wave simulation to obtain the electric field of the FW at the TMDs monolayer, and then used the excited second-order nonlinear polarizability as a secondary source for simulation with SHW.

Section 2: Field distribution of FW and SHW with homogeneous WS_2 monolayer

Figure S1 shows the field distribution of FW and SHW with homogeneous WS_2 monolayer on top of the photonic grating slab. The FW is launched from the top side with $K_x = 0.01K_a$, and the thickness of the grating slab is set to meet the doubly resonant condition. From the result, we see that the pair of BICs modes are excited successfully.

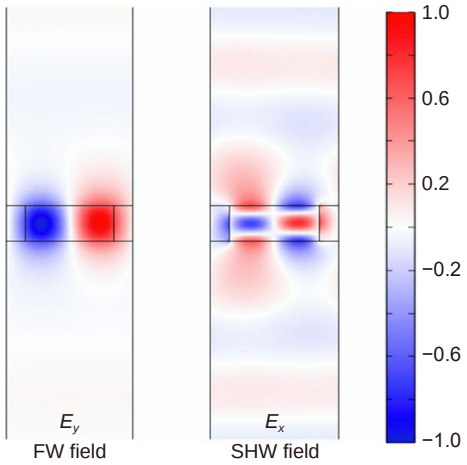

Fig. S1 | The electric field distribution of the FW and the SHW in a unit cell at $K_x = 0.01K_a$, respectively. It is seen that the paired BIC resonant modes are excited with a homogeneous TMD monolayer on top of the grating slab. Note that the field is normalized by the peak value in the figure. The TMD monolayer is only 0.618 nm, and thus is not visible due to the limited resolution of the figure.

Section 3: Field distribution of FW and SHW with patterned WS_2 monolayer

Figure S2 shows the field distribution of FW and SHW with a patterned WS_2 monolayer on top of the photonic grating

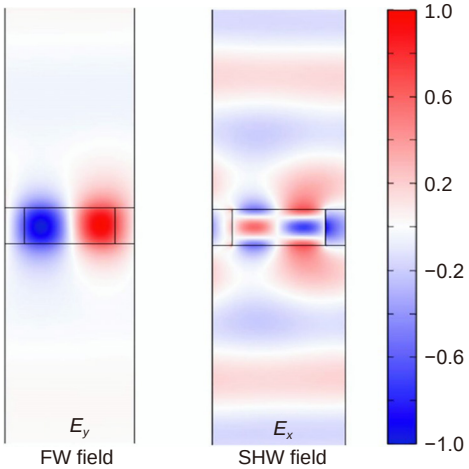

Fig. S2 | The electric field distribution of the FW and the SHW in a unit cell at $K_x = 0.01K_a$, respectively. It is seen that the paired BIC resonant modes are excited with a patterned TMD monolayer on top of the grating slab. Note that the field is normalized by the peak value in the figure. The TMD monolayer is only 0.618 nm, and thus is not visible due to the limited resolution of the figure.

slab. The FW is launched from the top side with $K_x = 0.01K_a$, and the thickness of the grating slab is set to meet the doubly resonant condition. One can see that the pair of BICs modes are excited successfully.

Section 4: Asymmetric outcoupling rate of TE-type BIC

By patterning the WS_2 monolayer, the mirror symmetry of the unit cell along x direction gets broken. Therefore, it leads to asymmetric SHG efficiency upon K_x. To show this asymmetric behavior, we have calculated the outcoupling rate to the top side of the grating slab for the TE-type BIC, and get the radiative quality factor $Q_{top}^{rad} = \omega \Big/ \left(2\gamma_{top}^{rad}\right)$ related to this top-side outcoupling rate γ_{top}^{rad}. The result is shown in Fig. S3. One can see that Q_{top}^{rad} at $-|K_x|$ is larger than that at $|K_x|$. This asymmetric behavior makes the field enhancement at WS_2 monolayer different upon K_x as shown in Fig. S4, giving rise to the asymmetric SHG efficiency.

Moreover, due to the mirror symmetry breaking with patterned WS_2 monolayer, the peak value of Q_{top}^{rad} does not appear at $K_x = 0$ as shown in Fig. S3, and therefore significant outcoupling rate exists, which leads to a significantly enhanced SHG efficiency at $K_x = 0$ as compared to the situation with homogeneous WS_2 monolayer.

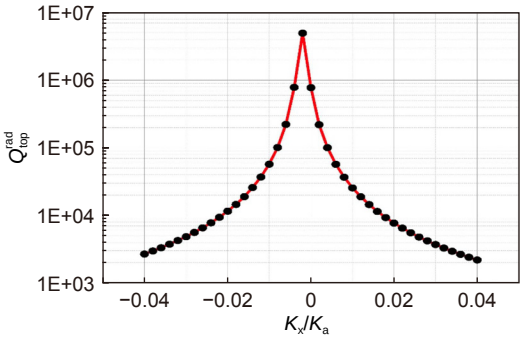

Fig. S3 | Radiative quality factor related to the top-side out coupling v.s. K_x. It is seen that the quality factor Q_{top}^{rad} at $-|K_x|$ is larger than that at $|K_x|$.

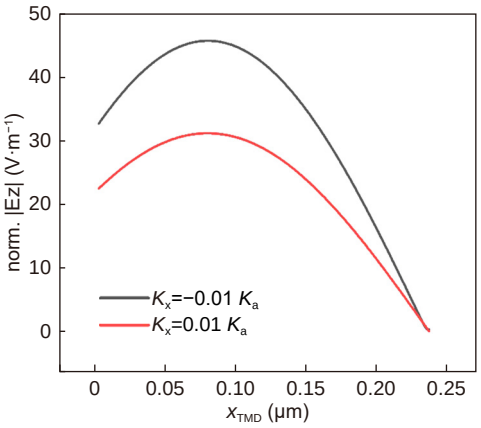

Fig. S4 | Field enhancement of pump light due to the BIC at different K_x. x axis represents the position on WS_2 monolayer with the origin started from the left edge of the WS_2 monolayer in a unit cell. y axis represents the electric field normalized by the amplitude of incident pump light. It is seen that the field enhancement is larger with incident vector $K_x = -0.01K_a$ than that with $K_x = 0.01K_a$, leading to a relatively larger SHG efficiency at $K_x = -0.01K_a$ as compared to that at $K_x = 0.01K_a$.

Section 5: Quality factor of quasi-BIC for a finite size grating

The finite size of a real 3D device will influence and lower the Q-factor due to the lattice perturbations at the edge breaking the coherence and leading to light scattering into free space[S1,S2]. To check the finite size effect on the quality factor, we model a grating slab of finite number unit cells, and check the quality factor by changing the number of unit cells. A finite size grating of 5 unit cells is shown in Fig. S5(a). Note that, the length of the grating strip (along y axis) is assumed much longer, and is modeled as infinite length.

In the simulation, we focused on the TE-type quasi-BIC mode at $K_x = 0.01K_a$, as shown in Fig. 1(c) in the manuscript. The quality factor for the infinite periodical grating is 18564. To check the quality factor of the finite size grating slab, we inserted one emitter into each unit cell of the grating, and set the frequency of light field f_r to be the eigen frequency of the quasi-BIC mode at $K_x = 0.01\ K_a$. Moreover, the phase of the emitters is set as $\Phi(x) = 0.01K_a{*}x$ for exciting the quasi-BIC eigen mode at $K_x = 0.01\ K_a$. After doing full wave simulation, the quality factor can be computed by using the formula $Q = 2\pi{*}f_r\ {*}\ W_{in}/P_{out}$, where W_{in} is the total energy of light field confined by the grating slab, and P_{out} is the total power leaking out the grating slab. The result is shown in Fig. S5(b). From the result, we see that the quality factor increases with the number of unit cells, and is larger than 10000 when reaching 45 unit cells. It indicates that a finite size grating with several tens of unit cells can give rise to a high quality factor. Fig. S5(c) shows the electric field distribution for a grating of 9 unit cells, which shows that the quasi-BIC mode has been successfully excited in the simulation.

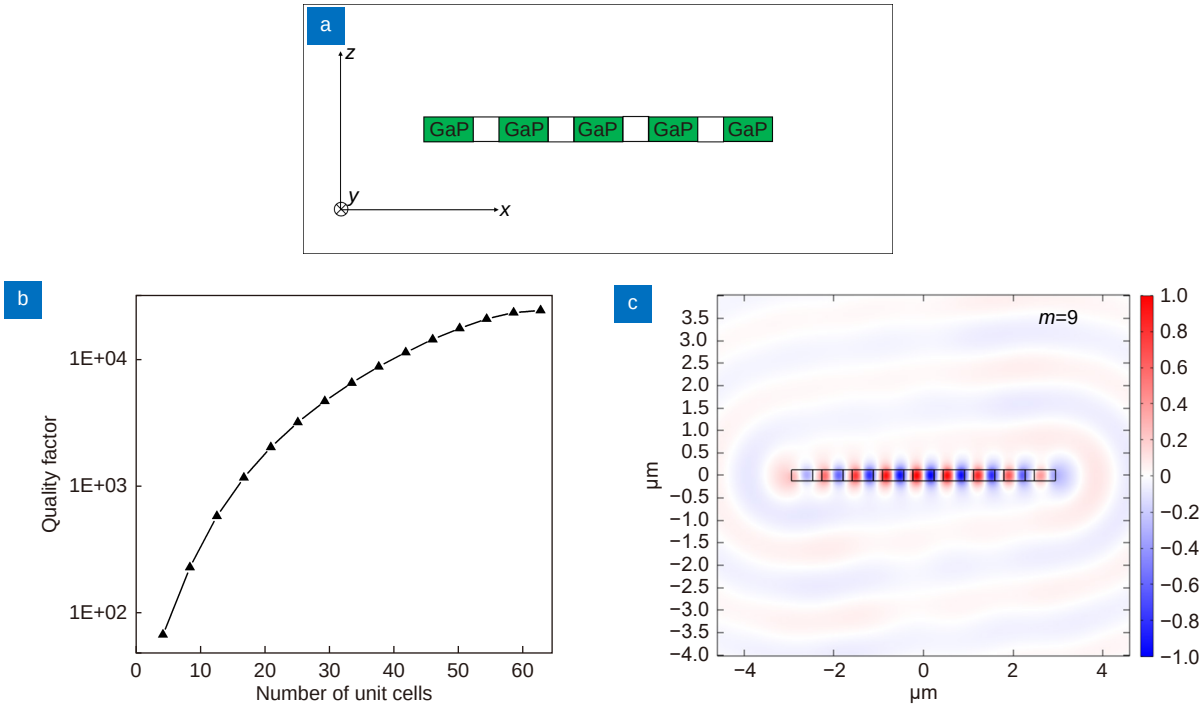

Fig. S5 | (**a**) An example of the modeled finite size grating slab with 5 unit cells. (**b**) Quality factor of the photonic grating slab with a finite number of unit cells. When the number of unit cell increases to 45, the quality factor of the finite size grating slab is larger than 1E4, and this value is close to the quality factor of an infinite periodical grating slab that is 1.8564E4 at $K_x = 0.01K_a$. (**c**) An example of field distribution of finite size grating slab with 9 unit cells. One sees that the quasi-BIC mode is successfully excited in the simulation.

Section 6: A flow chart for designing the dual BICs scheme

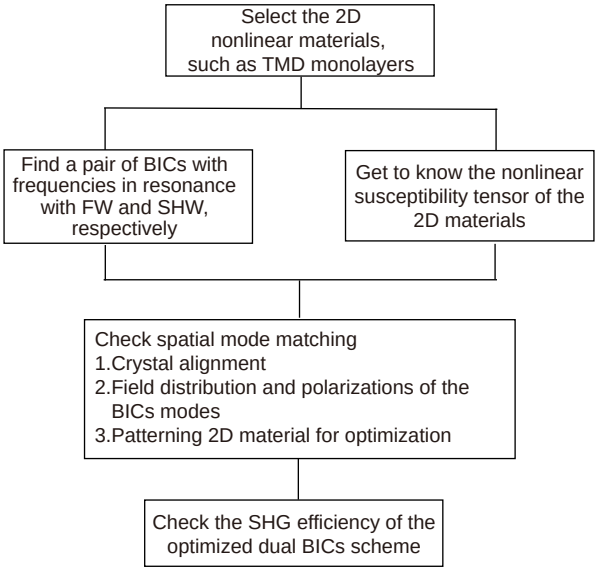

Fig. S6 | A flow chart for designing dual BICs scheme in other photonic structures.

Section 7: TMDs monolayer orientation-dependent polarization-resolved SHG efficiency

The polarization of the SHG signals in the dual BICs scheme should be related to the crystal orientation of the TMDs monolayer. To explore this effect in the dual BICs scheme, we fix the polarization of FW to *y* direction for successfully exciting the BIC mode, and meanwhile intentionally rotate the TMDs monolayer. Then, the polarization of the SHG signal is resolved by monitoring the power of *x*-polarized part and that of the *y*-polarized part simultaneously. The result for the case with a homogeneous TMD monolayer is shown in Fig. S7(a). From the result, we see that the SHG signal is polarized along *x* axis when the armchair direction is aligned with the *x* axis of the grating slab. When rotating to {30, 90, 150} degrees, the SHG signal is polarized along *y* axis. Note that the *x*-polarized SHG is related to the pair of BICs, while the *y*-polarized SHG is only related to the TE-type BIC (in resonant with the FW). For the case with patterned TMDs monolayer, since the spatial mode matching is optimized, the *x*-polarized SHG signal is significantly enhanced, making it much stronger than the *y*-polarized SHG signal, as shown in Fig. S7(b). Consequently, the SHG signal is most of *x* polarization, and is only polarized along *y* axis at several particular rotation angles of {30, 90, 150} degrees.

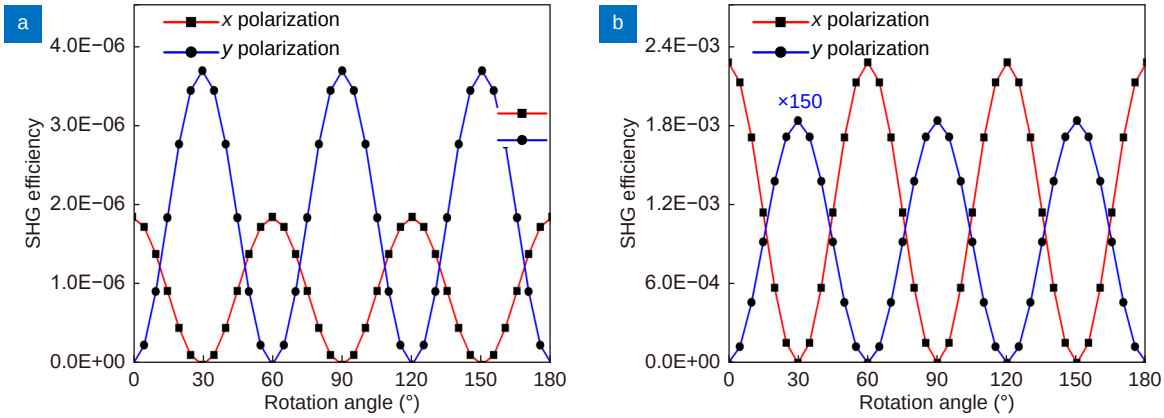

Fig. S7 | Change of *x*-polarized and *y*-polarized SHG signal upon the rotation angle between the TMDs armchair direction and the *x* axis of the grating slab. (**a**) Polarization-resolved SHG efficiency for BICs grating slab covered by a homogeneous TMDs monolayer. Here the quasi-BIC at $K_x = 0.08K_a$ is excited. (**b**) Polarization-resolved SHG efficiency for BICs grating slab covered by the patterned TMDs monolayer. Note that here the *y*-polarized signal is magnified by 150 times for better visibility. Here the quasi-BIC at $K_x = -0.06K_a$ is excited. In the figures, the SHG signal is collected at the reflection side of the grating slab, and SHG signal at the transmission side behaves in the same way.

Section 8: SHG efficiency of homogeneous bulk GaP

Since GaP is noncentrosymmetric material, it may exhibit SHG under appropriate condition. The (100)-grown GaP has a second order nonlinear susceptibility χ_{ijk} $(i \neq j \neq k)$. Therefore, with the crystal axis (x',y',z') aligned as (x,y,z) coordinate axis in the manuscript, it does not exhibit SHG with y-polarized incident pump light.

In a different configuration, i.e. by rotating the polarization of pump light to 90 degree (x-polarized), and meanwhile scanning the incident angle in the x-z plane, a homogeneous bulk (100)-GaP slab may exhibit SHG, and the result is shown in Fig. S8. It is seen that the maximum SHG efficiency from GaP is achieved at a relatively large incident angle (>50 deg), reaching ~10^{-8} at the reflected side and ~2×10^{-8} at the transmitted side, respectively. In comparison, by employing doubly resonant BICs, the homogeneous monolayer of WS_2 exhibits SHG efficiency about two order larger, reaching ~2×10^{-6} at both the reflected and transmitted sides. Moreover, the proposed patterning strategy leads to an extra ~10^3 times enhancement with WS_2 monolayer in the dual BICs scheme.

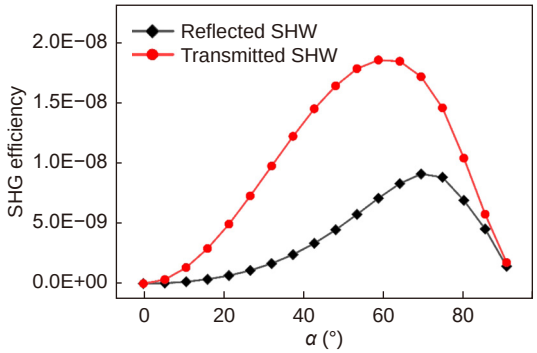

Fig. S8 | SHG efficiency of GaP v.s. incident angle *α* of pump light. Here, the polarization of the pump light is no longer in the y direction as in the main text, but is in the x-z plane for successfully exciting the SHW. The intensity of incident pump light is again set to be 0.1 GW/cm^2, and the second-order nonlinear susceptibility χ_{ijk} is set to be 100 pm/V, which is the same as that of the WS_2 monolayer for comparison. The thickness of GaP slab is set to be t = 0.36875 a, which is the value that fulfills the doubly resonant condition at $K_x = 0.01K_a$.

Section 9: Prospectives for experimental realizations

Although this research work is a theoretical prediction, other research works have already demonstrated the potentials for realizing such systems experimentally. Placing 2D materials onto photonic structure can be realized by employing dry transfer technique[S3,S4], while photonic grating can be prepared by standard nanofabrication methods[S5]. Moreover, the optical patterning of 2D materials has received enormous interest and emerged as a hot topic in recent years due to their unique electronic and photonic properties associated with various potential applications. Thus a variety of optical techniques can be potentially employed to realize the proposed TMD monolayer structure, including laser thinning, doping, phase transition, oxidation, ablation, etc.[S6–S8].

References

S1. Fedotov VA, Papasimakis N, Plum E, Bitzer A, Walther M et al. Spectral collapse in ensembles of metamolecules. *Phys Rev Lett* **104**, 223901 (2010).
S2. Jenkins SD, Ruostekoski J. Metamaterial transparency induced by cooperative electromagnetic interactions. *Phys Rev Lett* **111**, 147401 (2013).
S3. Castellanos-Gomez A, Buscema M, Molenaar R, Singh V, Janssen L et al. Deterministic transfer of two-dimensional materials by all-dry viscoelastic stamping. *2D Mater* **1**, 011002 (2014).
S4. Masubuchi S, Morimoto M, Morikawa S, Onodera M, Asakawa Y et al. Autonomous robotic searching and assembly of two-dimensional crystals to build van der Waals superlattices. *Nat Commun* **9**, 1413 (2018).
S5. Rahmani M, Leo G, Brener I, Zayats AV, Maier SA et al. Nonlinear frequency conversion in optical nanoantennas and metasurfaces: materials evolution and fabrication. *Opto-Electron Adv* **1**, 180021 (2018).
S6. Stanford MG, Rack PD, Jariwala D. Emerging nanofabrication and quantum confinement techniques for 2D materials beyond graphene. *npj 2D Mater Appl* **2**, 20 (2018).
S7. Kollipara PS, Li JG, Zheng YB. Optical patterning of two-dimensional materials. *Research* **2020**, 6581250 (2020).
S8. Guo YF, Shen PC, Su C, Lu AY, Hempel M et al. Additive manufacturing of patterned 2D semiconductor through recyclable masked growth. *Proc Natl Acad Sci USA* **116**, 3437–3442 (2019).